Limiting Factors to the Temperature Performance of THz Quantum Cascade Lasers Based on the Resonant-Phonon Depopulation Scheme

Y. Chassagneux, Q. J. Wang, S. P. Khanna, E. Strupiechonski, J.-R. Coudevylle, E. H. Linfield, A. G. Davies, F. Capasso, M. A. Belkin, and R. Colombelli

(Invited Paper)

***Abstract*—We analyze the temperature performance of five terahertz (THz)-frequency quantum cascade lasers based on a three-quantum-well resonant-phonon depopulation design as a function of operating frequency in the 2.3–3.8-THz range. We find evidence that the device performance is limited by the interplay between two factors: 1) optical phonon scattering of thermal electrons, which dominates at shorter wavelengths, and 2) parasitic current, which dominates at longer wavelengths. We present a simple model that provides an accurate estimate of the parasitic current in these devices and predicts the dependence of the threshold current density on temperature.**

***Index Terms*—Quantum cascade lasers (QCLs), semiconductor lasers, terahertz (THz).**

I. INTRODUCTION

PRACTICAL terahertz (THz) frequency systems for imaging, sensing, and spectroscopy would benefit from the development of compact, efficient electrically pumped sources. One of the most promising sources is the THz quantum cascade laser (QCL) [1]. Since their initial demonstration in 2001 [2], there has been remarkable progress in the development of these devices. Currently, THz QCLs have been shown to operate at frequencies from 1.2 to 5 THz (down to 0.85 THz in large magnetic fields) and to produce continuous-wave (CW) output powers $>$100 mW [1]. Furthermore, the emission linewidth of distributed-feedback THz QCLs is only a few tens of kilohertz, making them ideal local oscillators for heterodyne detection [3], [4].

However, THz QCLs have yet to achieve room-temperature operation. The maximum operating temperature $(T_{\max})$ demonstrated to date, without a magnetic field, is 186 K [5] for pulsed operation and 117 K for CW operation [6]. With an applied magnetic field of 20–30 T, THz QCLs can operate to higher temperatures, with $T_{\max} = 225$ K demonstrated for 3-THz devices [7]. Recently reported THz QCL designs based on scattering-assisted electron injection [8] and double-phonon depopulation [9] show promise to increase $T_{\max}$ further, but have not yet achieved record operating temperatures. A summary of the temperature performance of a number of THz QCLs (taken from the literature and operating without a magnetic field) as a function of frequency is shown in Fig. 1(a). The improvement in temperature performance has been rapid after their initial demonstration, but it has slowed down considerably in recent years, as shown in Fig. 1(b). The trend in Fig. 1(b) suggests the presence of physical mechanism(s) preventing operation of current designs at higher temperatures. Several temperature-activated processes have been suggested to cause the degradation of the laser gain with temperature: thermal backfilling of the lower laser state, optical phonon scattering of thermal electrons in the upper laser state, decrease of the injection efficiency in the upper laser state, and increase of the waveguide losses with temperature [1], [10].

In this paper, we elucidate the limits to the temperature performance of THz QCLs with active regions based on the three-quantum-well (3QW) resonant-phonon depopulation scheme [11], [12]. Five THz QCLs operating at frequencies of 2.3, 2.8, 3.1, 3.5, and 3.8 THz are compared. The dependence of the threshold current densities $(J_{\rm th})$ with the heat-sink temperature indicates that the performance of these devices is limited by the interplay of two factors: 1) optical phonon scattering of thermal electrons, which dominates at shorter wavelengths, and 2) parasitic current, which dominates at longer wavelengths.

Manuscript received July 14, 2011; revised August 30, 2011; accepted September 01, 2011. Date of publication December 22, 2011; date of current version January 18, 2012. The work of R. Colombelli, Y. Chassagneux, E. Strupiechonski, and J.-R. Coudevylle was supported in part by a EURYI scheme award (www.esf.org) and the French National Research Agency (ANR-09-NANO-017 "Hi-Teq"). The nano-center CTU-IEF-Minerve is funded in part by the "Conseil Général de l'Essone." Harvard-CNS is a member of the National Nanotechnology Infrastructure Network. The work of S. P. Khanna, E. H. Linfield, and A. G. Davies was supported in part by the EPSRC (UK) and the EC project NOTES. The work of F. Capasso, M. A. Belkin, and Q. J. Wang was supported by the Air Force Office of Scientific Research under Contract FA9550-09-1-0505. The work of M. A. Belkin, was also supported in part by the National Science Foundation under Grant ECCS-0935217 and the Texas Higher Education Coordinating Board "Norman Hackerman Advanced Research Program" Award.

Y. Chassagneux, E. Strupiechonski, J.-R. Coudevylle, and R. Colombelli are with the Institut d'Electronique Fondamentale, Univ. Paris Sud and CNRS, UMR8622, 91405 Orsay, France (e-mail: raffaele.colombelli@u-psud.fr).

Q. J. Wang and F. Capasso are with School of Engineering and Applied Sciences, Harvard University, Cambridge, MA 02138 USA.

S. P. Khanna, E. H. Linfield, and A. G. Davies are with the School of Electronic and Electrical Engineering, University of Leeds, Leeds LS2 9JT, U.K.

M. A. Belkin is with the Department of Electrical and Computer Engineering, The University of Texas at Austin, Austin, TX 78758 USA (e-mail: mbelkin@ece.utexas.edu).

Color versions of one or more of the figures in this paper are available online at http://ieeexplore.ieee.org.

Digital Object Identifier 10.1109/TTHZ.2011.2177176

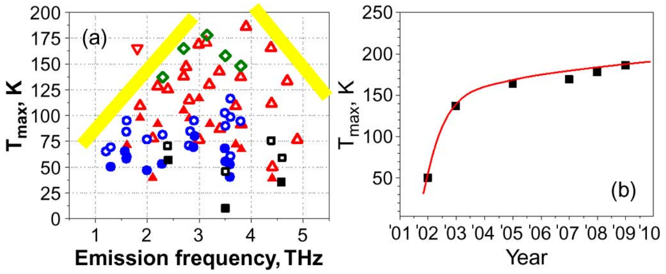

Fig. 1. (a) Summary of the maximum operating temperatures of THz QCLs reported to date. Solid symbols refer to CW operation, and open symbols refer to pulsed operation. Green diamonds refer to the devices presented in this paper, red upright triangles are resonant-phonon designs, a red upside-down triangle at 1.8 THz is recently reported scattering-assisted injection design [8], blue circles refer to bound-to-continuum designs, and black squares are chirped superlattice designs. (b) Timeline for $T_{\max}$ in pulsed mode achieved by THz QCLs. The data are taken from [5], [7], [10].

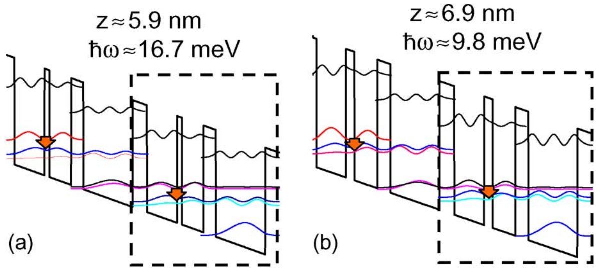

Fig. 2. Conduction band structure of the 3QW design for the (a) 3.8-THz structure and for the (b) 2.3-THz structure. The layer structure and doping are indicated in the text.

These factors result in an optimal frequency ("*sweet spot*") around 3 THz for lasers based on this design. We develop a simple semi-phenomenological model which can be used to estimate the parasitic current accurately in such devices and to predict the dependence of $J_{\rm th}$ on the heat-sink temperature.

II. ACTIVE REGION DESIGN AND DEVICE FABRICATION

Fig. 1(a) indicates that there are limiting factors controlling $T_{\max}$ at both low and high frequencies (as illustrated by the thick yellow lines). This results in a sweet spot between 2.5–3.5 THz, where QCLs achieve the highest $T_{\max}$. A systematic study of devices based on the same design, but operating at different frequencies, may allow one to elucidate the phenomena involved.

We employed the 3QW design originally developed in [11], since this structure [12] and its derivatives [5], [10] exhibit the best temperature performances to date. We designed five different THz QCLs with nominal emission frequencies of 2.3, 2.7, 3.1, 3.5 and 3.8 THz. In order to allow for the results to be compared, great care was taken to keep the laser designs very similar. All devices exploit a vertical lasing transition and the laser states' anticrossing energies with injection/extraction levels were kept nearly the same (approximately 2 meV splitting at the injection and 4 meV at the extraction). The structures were grown by molecular beam epitaxy (MBE) on undoped GaAs substrates; the growth sequence comprised a 250-nm-thick undoped GaAs buffer layer, followed by a 300-nm-thick $\rm Al_{0.5}Ga_{0.5}As$ etch-stop layer, a 75-nm-thick layer of GaAs n-doped to 5×10^{18} $\rm cm^{-3}$, a 10-μm-thick active region containing multiple QCL cascades (219–226 periods for the different laser designs), and finally a 50-nm-thick GaAs layer n-doped to 5×10^{18} $\rm cm^{-3}$. The active regions in all devices used the $\rm GaAs/Al_{0.15}Ga_{0.85}As$ material system. The layer sequences, starting from the injection barrier, are **48**/95/**27**/73/**42**/157 Å (2.3 THz design), **48**/94/**24**/72/**42**/157 Å (2.7 THz design), **48**/96/**20**/74/ **42**/161 Å (3.1 THz design), **47**/98/**17**/74/**41**/162 Å (3.5 THz design), and **47**/99/**15**/73/**40**/164 Å (3.8 THz design), where the barriers are indicated in bold. The center third (50 Å) of each injector well was n-doped to 5×10^{16} $\rm cm^{-3}$. Fig. 2 shows the conduction band structure of two periods of the devices designed for emission at 3.8 THz [Fig. 2(a)] and 2.3 THz [Fig. 2(b)].

The samples were grown in the same MBE machine using similar growth conditions. After gold–gold thermo compression wafer bonding and substrate removal, the lasers were processed into standard metal–metal ridge waveguides with Ti (10 nm)/Au cladding. The laser ridges were processed both by wet etching, resulting in larger ridges (80/140/200/300 μm wide), and by dry etching, resulting in narrower ridges (50/75/90/100/125/150 μm wide). $J_{\rm th}$ and $T_{\max}$ in pulsed operation obtained from the wet and dry-etched devices are similar.

After substrate thinning and back-contact deposition, the devices were cleaved into laser bars (1.5 to 2 mm long), soldered on copper blocks, and mounted in a cryostat for characterization. Devices were operated in pulsed mode with 50–300-ns current pulses and with duty cycles $<1\%$. The emission wavelengths in all devices were in good agreement with the target frequencies. The top figure of Fig. 3 shows typical laser spectra for a device from each wafer at 80 K.

III. FREQUENCY SWEET SPOT FOR MAXIMUM OPERATING TEMPERATURE

Although the active regions of the devices are very similar, the QCL behavior as a function of temperature strongly depends on the operating wavelength. The middle and bottom panels of Fig. 3 show the light–voltage–current $(L\text{–}V\text{–}I)$ characteristics at different heat-sink temperatures for the devices with the two extreme emission frequencies, 3.8 THz (middle plot of Fig. 3) and 2.3 THz (bottom plot of Fig. 3). As seen in the middle and bottom plots of Fig. 3, the dynamic ranges at low temperatures for these two devices are very different. However, despite this, both devices exhibit similar $T_{\max}$, in the 130–140 K range. A summary of $J_{\rm th}$ as a function of the heat-sink temperature for all devices is presented in Fig. 4. We note that all lasers demonstrated very good temperature performance, comparable or better than the current state of the art [see Fig. 1(a)].

As indicated in Fig. 4, the highest operating temperatures were obtained for devices operating at frequencies 2.8 and 3.1 THz, in agreement with the literature [Fig. 1(a)]. Fig. 4 suggests that two separate factors limit the performance of THz QCLs at higher/lower frequencies. On the low-frequency side, the dramatic increase in $J_{\rm th}$ at low temperature (from 550 $\rm Acm^{-2}$ at

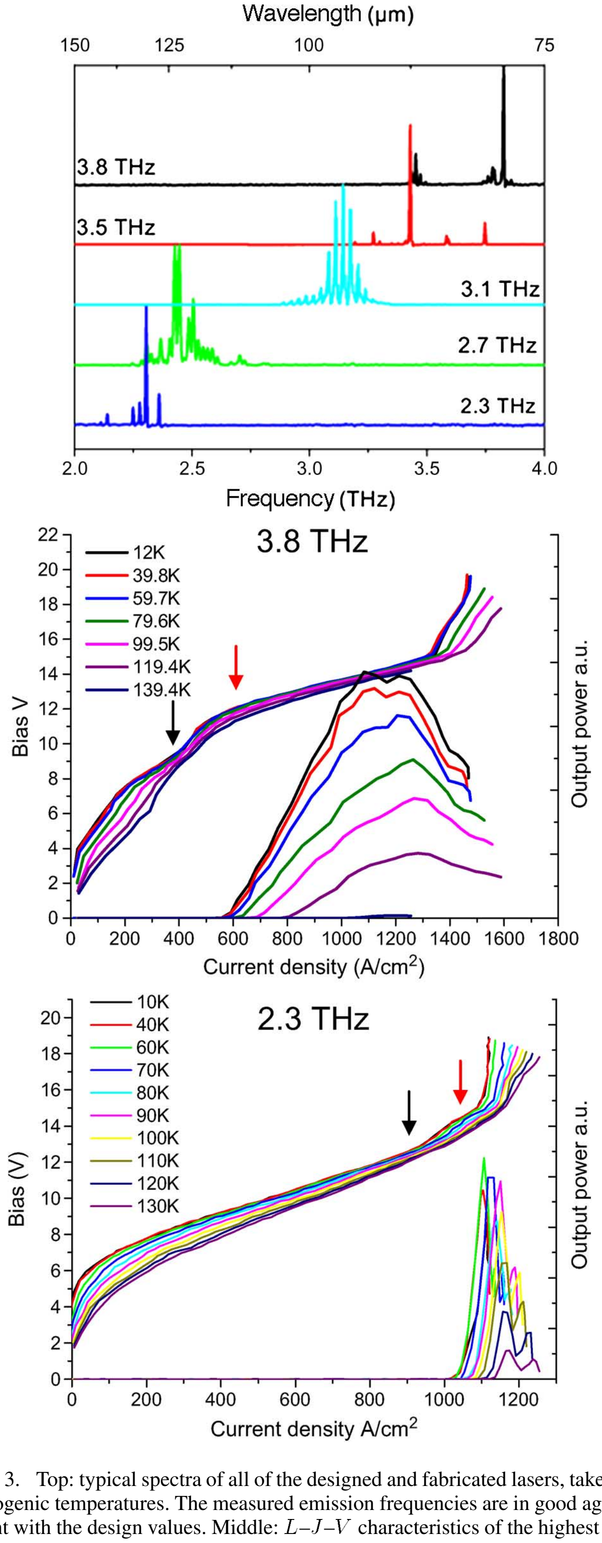

Fig. 3. Top: typical spectra of all of the designed and fabricated lasers, taken at cryogenic temperatures. The measured emission frequencies are in good agreement with the design values. Middle: L–J–V characteristics of the highest frequency laser, which operates at $\nu \approx$ 3.8THz. The black arrows show the approximate value of the parasitic current density (J_{par}), while the red arrows mark approximately the nominal lasing threshold. Bottom: L–J–V characteristics of the lowest frequency laser, which operates at $\nu \approx$ 2.3THz. It is clear that the dynamic range decreases with the operating frequency.

3.8 THz to 1050 Acm^{-2} at 2.3 THz) reduces the available dynamic range. On the high-frequency side, the laser J_{th} increases more rapidly with heat-sink temperature with increasing device frequency. We present a simple semi-phenomenological model which accurately predicts the dependence of J_{th} on temperature for all the lasers in this study, as well as for the 3QW QCL design with a diagonal lasing transition reported in [5].

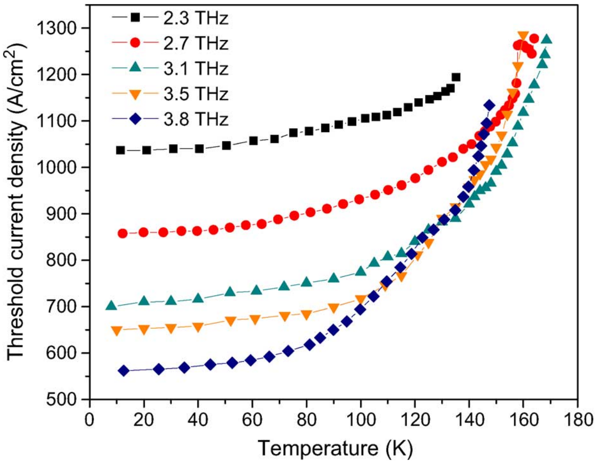

Fig. 4. Experimental threshold current density (J_{th}) as a function of the heat-sink temperature, for the five similar three active well designs. Each laser operates at a different lasing frequency. The highest $T_{\max}$ is obtained for the laser operating at $\nu = 3.1$ THz.

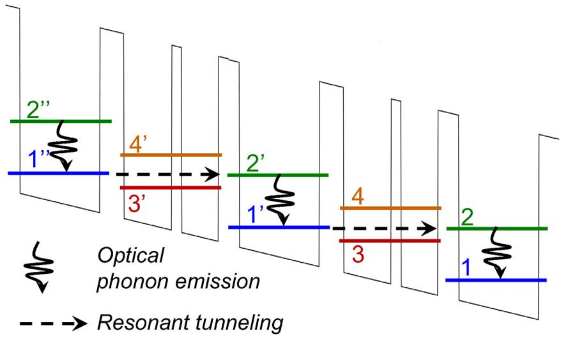

Fig. 5. Schematic of the level alignment at the parasitic bias. The electrons tunnel *through* the active region without emission of photons. Only phonon emission takes place in the large wells. The electronic transport in this configuration can be described with a simple tight-binding model [13], [14]

IV. LOW-FREQUENCY LIMIT: "PARASITIC" CURRENT

The middle and bottom plots of Fig. 3 demonstrate that the laser dynamic range decreases as the emission frequency is reduced. The current–voltage (I–V) characteristics of the devices in the middle and bottom plots of Fig. 3 suggest that a larger fraction of the injected current flows at a lower bias voltage with respect to the design bias, up to a voltage point (indicated by black arrows in the middle and bottom plots of Fig. 3), when the structure starts to align towards the correct design laser bias, which is marked by the red arrows.

In both figures, as the bias is increased, there is an initial alignment of the band-structure (marked by the black arrows) where electrons are assumed to flow by emitting LO-phonons only, as shown schematically in Fig. 5. This bias is *below* the nominal design bias (marked with red arrows). At this initial alignment, there is a parasitic current density, J_{par}, which is a large fraction of J_{th} in the lower frequency QCL design. We assume that J_{par} corresponds to electron transport across the structure based on resonant tunneling *through* the active region

TABLE I

ANTICROSSING ENERGY AT THE PARASITIC ALIGNMENT ($\Delta_{1'2}$), CALCULATED AND EXPERIMENTAL $J_{\rm par}$ FOR THE DIFFERENT LASER DESIGNS. IT IS CLEAR THAT $J_{\rm par}$ DEPENDS ON THE LASER FREQUENCY VIA THE DEPENDENCE OF THE ANTICROSSING ENERGY ON THE POSITION OF LEVELS 3 AND 4, WHICH ARE SEPARATED BY THE ENERGY OF A LASER PHOTON. THE AGREEMENT BETWEEN THE MODELING AND THE EXPERIMENT IS VERY GOOD

v (THz)	2.3	2.7	3.1	3.5	3.8
$\Delta_{1'2}$ (meV)	1.08	0.94	0.79	0.74	0.68
J_{par} (calc.)	**1025** (Acm^{-2})	**876**	**701**	**640**	**566**
J_{par} (exp.)	**991±54**	**872±73**	**632±70**	**508±70**	**462±70**

from state $1'$ to state 2 (see Fig. 5) with a subsequent electron relaxation to state 1. If we assume that the tunneling from state $1'$ to state 2 is coherent through the entire active region, we can use a simple tight-binding model [13], [14] to describe the current flow. As a matter of fact, the coherence of the electronic transport in THz QCLs is still a hot topic of study [15], [16].

Following [13] and [14], at the QCL alignment shown in Fig. 5, the system operates in the so-called *weak-coupling* regime. $J_{\rm par}$ can be approximated as

$$J_{\rm par} = \frac{eN}{2} \cdot \frac{(\Delta_{1'2}/\hbar)^2 \tau_{//}}{\left(1 + (\Delta_{1'2}/\hbar)^2 \tau_{//} \tau\right)} \qquad (1)$$

where $\Delta_{1'2}$ is the anticrossing energy between levels $1'$ and 2 at the parasitic alignment (computed in the extended basis which comprises three QWs, i.e., the real structure), N is the doping density (most of the electron population is in the ground injector state, state $1'$), τ is the phonon emission time in the upper injector state (state 2), and $\tau_{//}^{-1} = (1/2\tau) + (1/T_2^*)$, where T_2^* is a pure dephasing time.

At a first intuitive look, the value of $\Delta_{1'2}$ is expected to be similar for all structures tested. However, a more careful analysis reveals that this is inaccurate, since the coupling between levels $1'$ and 2 depends strongly on the position of levels 3 and 4, which are separated by the energy of a laser photon [1], [23]. As a result, $\Delta_{1'2}$ (calculated within a Schrödinger–Poisson approach), and—crucially—$J_{\rm par}$, depend on the laser frequency, as shown in Table I.

The values of $J_{\rm par}$ can be experimentally determined from the device I–V characteristics as the points where the second derivative of V as a function of I is zero (or where the differential resistance is *locally* maximal). These are the previously discussed positions in the middle and bottom plots of Fig. 3 indicated by the black arrows. The values of $J_{\rm par}$ at 80 K obtained for all devices tested are listed in Table I. The values of τ and $\tau_{//}$ in (1) can now be adjusted to reproduce the experimental $J_{\rm par}$. We find that (1) can correctly fit $J_{\rm par}$ for all devices with $\tau \approx 1.0$ ps and $\tau_{//} \approx 0.325$ ps, as shown in Table I. The value of $\tau_{//}$ is similar to that reported in [5], while the value of $\tau \approx 1.0$ ps is close (albeit somewhat larger) to the expected electron lifetime in a state with resonant phonon depopulation.

Overall, this analysis suggests that the limitation for low-frequency operation of 3QW THz QCLs based on resonant-phonon depopulation can be explained by the presence of a parasitic tunneling current. We note that similar ideas have been discussed, e.g., in [5] and [6].

V. HIGH-FREQUENCY LIMIT: LO-PHONON EMISSION BY HOT ELECTRONS

Fig. 4 shows the evolution of $J_{\rm th}$ as a function of the heat-sink temperature, which we assume to be equal to the electron temperature. This is not exactly the case, as shown in [17], but it represents a reasonable approximation here. Fig. 4 provides experimental evidence that the higher is the operating frequency of the device, the faster is the increase of $J_{\rm th}$ with temperature. The dependence on laser operating frequency excludes thermal backfilling of the lower laser state, and any increase in waveguide losses with temperature, as possible dominant causes. On the other hand, LO-phonon scattering of thermally excited electrons [1], [10] from the upper to the lower laser state is a good candidate to explain the observed dependence of $J_{\rm th}$ on temperature [1]. This process depends both on the temperature and on the photon energy, as the electrons in the upper laser state need to acquire an in-plane kinetic energy equal to the difference between the phonon and photon energies. This allows them to emit an LO phonon and be scattered to the lower laser state.

The emission rate $(W_{\rm emi})$ for the process of LO phonon scattering of thermally excited electrons can be expressed as

$$W_{\rm emi}(T) = \frac{\int W(k) f_{\rm FD}(E_k) dE_k}{\int f_{\rm FD}(E_k) dE_k} \qquad (2)$$

where E_k is the in-plane kinetic energy of an electron, $W(k)$ the LO-phonon emission rate as a function of in-plane momentum, and $f_{\rm FD}$ the Fermi–Dirac distribution. When the energy separation between the upper and lower laser levels is less than the LO-phonon energy $(E_{\rm LO})$, and the electron density in state 2 is low so that the Fermi energy is much smaller than $k_B T$ (which is indeed our case), the emission rate can be approximated as

$$W_{\rm emi}(T) \approx W_{\rm hot} \cdot e^{\frac{(h\nu - E_{\rm LO})}{k_B \cdot T_e}} \qquad (3)$$

where $W_{\rm hot}$ is independent of the temperature, k_B is the Boltzmann constant, and T_e is the electron temperature [17].

If the temperature dependence of $J_{\rm th}$ in our devices is indeed mostly governed by the LO phonon scattering of thermally excited electrons, then the evolution of $J_{\rm th}$ with temperature should follow the same activated behavior as in (3). In Fig. 6, we plot $J_{\rm th}$ as a function of the activation term $\exp[(h\nu - E_{\rm LO})/k_B T]$, instead of the heat sink temperature, for all devices. The curves are now almost parallel, providing a convincing evidence that the dominant thermal process in our devices is the activated LO phonon emission. The curves in Fig. 6 do not overlap since the parasitic current is different for each device, as discussed previously. If we subtract the values of $J_{\rm par}$ (Table I) from the curves in Fig. 6, all of the data can collapse onto a single curve (Fig. 7), which further corroborates our model.

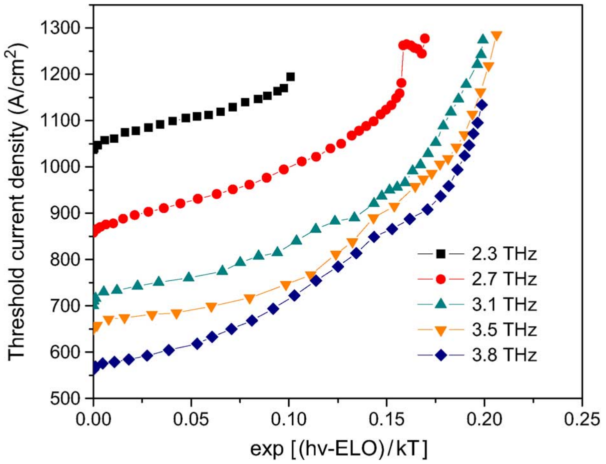

Fig. 6. Experimental $J_{\rm th}$ for the different laser devices plotted as a function of the activation term (which is $\exp(-(E_{\rm LO} - h\nu)/k_BT))$. The frequencies used for the plot are 2.3, 2.7, 3.1, 3.5, and 3.8 THz, respectively for the different laser devices (as shown in the legend).

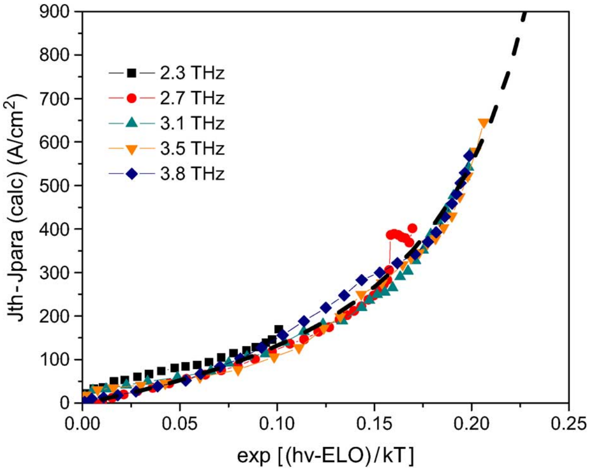

Fig. 7. Experimental $(J_{\rm th} - J_{\rm par})$ as a function of the activation term Note: the $J_{\rm par}$ values used are the calculated values from see Table I. The dashed black curve is the result of a fit to the data with Eq. (9). The fit parameters are $C = 252\ {\rm Acm}^{-2}$ and $\tau_1/\tau_{21,{\rm hot}} = 3.43$.

VI. MODELING THE DEPENDENCE OF THE THRESHOLD CURRENT DENSITY ON TEMPERATURE

We have established that: 1) the parasitic current can be inferred from the device structure, assuming coherent electron tunneling through the active region and 2) the temperature dependence of $J_{\rm th}$ is determined mostly by the LO-phonon scattering of thermal electrons in the upper laser state. We will now show that our semiphenomenological model allows us to estimate the dependence of $J_{\rm th}$ on temperature for a given laser design.

We assume that the parasitic current behaves as a parallel conduction channel which *does not disappear* when the laser's nominal operation bias is reached. Current injection in the upper laser level is therefore considered as a second, additional conduction channel, and $J_{\rm par}$ is simply an offset to the total injected current. This hypothesis will be justified *a posteriori* by the excellent agreement between this model and the experimental results (Fig. 7). To support this hypothesis further, we note that recent theoretical results based on nonequilibrium Green's functions suggest that a multibarrier coherent electron tunneling from one injector to the next may account for over 50% of the current flow in a four-quantum-well THz QCL *under operating bias* [15], [16]. This effect may be even more pronounced in our 3QW THz QCLs.

The population inversion can be approximated by considering the lasers as two-level systems, where level 2 corresponds to the upper laser state and level 1 to the ground state:

$$n_2 - n_1 = \frac{J_{\rm eff} \cdot (\tau_{21} - \tau_1)}{e} \tag{4}$$

where n_i is the electron population in state i, τ_1 is the electron lifetime in the lower laser level (in our case, it is determined by resonant tunneling into the injector and subsequent optical phonon scattering), τ_{21} is the electron scattering time from state 2 to state 1 (which is determined by optical phonon scattering of thermal electrons in state 2, see (3)), and $J_{\rm eff} = J - J_{\rm par}$.

The threshold current density $J_{\rm th}$ can be then expressed as follows:

$$J_{\rm th} = J_{\rm par} + \alpha_{\rm total} \cdot \left(\frac{\varepsilon_0 hcn_{\rm eff}}{4\pi e}\right) \cdot \left(\frac{\delta\nu}{\nu_0}\right) \cdot \frac{L_{\rm per}}{|z|^2} \cdot \frac{1}{\tau_{21} - \tau_1} \tag{5}$$

where α_{total} are the total optical losses in the laser, $n_{\rm eff}$ is the modal effective index, z is the optical dipole moment for the laser transition, c the speed of light in vacuum, e is the magnitude of the electron charge, $\delta\nu$ is the full-width at half-maximum (FWHM) of the laser transition at frequency ν_0, and $L_{\rm per}$ is the length of one period. Equation (5) can be rewritten in typical units used in experiments as

$$J_{\rm th}^{[{\rm A/cm}^2]} = J_{\rm par}^{[{\rm A/cm}^2]} + 31.5 \cdot \alpha_{\rm total}^{[{\rm cm}^{-1}]} \cdot \left(\frac{\delta\nu}{\nu_0}\right) \cdot \frac{L_{\rm per}^{[{\rm nm}]}}{|z^{[{\rm nm}]}|^2} \cdot \frac{1}{\tau_{21}^{[{\rm ps}]} - \tau_1^{[{\rm ps}]}}. \tag{6}$$

We can now introduce the temperature dependence of τ_{21} following (3) as

$$\frac{1}{\tau_{21}} = \frac{1}{\tau_{21,0}} + \frac{1}{\tau_{21,hot}} \cdot e^{\frac{h\nu - E_{LO}}{k_BT_e}} \tag{7}$$

where $\tau_{21,0}$ is the upper level lifetime at $T = 0$ K, and $\tau_{21,{\rm hot}} = 1/W_{\rm hot}$ is the lifetime of hot electrons in level 2 which can emit optical phonons and relax to level 1. Inserting (7) into (6) yields the following formula for the temperature dependence of $J_{\rm th}$:

$$J_{\rm th} = J_{\rm par} + \frac{C}{\tau_1} \cdot \left(\frac{1}{1 - \frac{\tau_1}{\tau_{21,0}} - \frac{\tau_1}{\tau_{21,{\rm hot}}} \cdot e^{\frac{h\nu - E_{LO}}{k_BT_e}}} - 1\right) \tag{8}$$

where C is $31.5 \cdot \alpha_{\rm total} \cdot (\delta\nu/\nu_0) \cdot (L_{per}/z^2)$. Furthermore, it can be safely assumed that $\tau_{21,0} \gg \tau_{21,{\rm hot}}$, which leads to

$$J_{\rm th} = J_{\rm par} + \frac{C}{\tau_1} \cdot \left(\frac{1}{1 - \frac{\tau_1}{\tau_{21,{\rm hot}}} \cdot e^{\frac{h\nu - E_{\rm LO}}{k_BT_e}}} - 1\right). \tag{9}$$

The dashed black line in Fig. 7 represents a fit to the experimental data using (9) and assuming the electron temperature is the same as the heat sink (lattice) temperature: the agreement is excellent and yields the following fit parameters:

$$\frac{C}{\tau_1} = 252 \text{ A/cm}^2$$
$$\frac{\tau_1}{\tau_{21,\mathrm{hot}}} = 3.43.$$

We can compare these "fitting" values with the ones obtained theoretically from known laser parameters. Using $\alpha_{\mathrm{total}} = 15$ cm^{-1}, $\delta\nu/\nu_0 = 0.20$, $L_{\mathrm{per}} = 44$ nm, $z = 6$ nm, and $\tau_1 = 0.8$ ps [18], we obtain a value of 144 Acm^{-2} for C/τ_1, which is in fair agreement with the fit. The value of $\tau_1/\tau_{21,\mathrm{hot}}$ can be estimated by taking the lifetime $\tau_{21,\mathrm{hot}} \approx 0.3$ ps in accordance with the lifetimes calculated and measured for resonant optical phonon scattering in quantum wells [19] and comparing it with a value of $\tau_1 \approx 0.8$ ps [18]. We obtain $\tau_1/\tau_{21,\mathrm{hot}} = 2.7$, which is in good agreement with the result of the fit.

Theoretical simulations [20], [21] and experimental measurements [17] suggest that the electron temperature of the upper laser state in THz QCLs is 50–100 K higher than the lattice temperature in devices based on the resonant-phonon depopulation designs. The simulations and experimental measurements were performed with QCLs operating at heat-sink temperatures $<$100 K. One may expect that the optical phonon scattering of thermal electrons may have a "cool down" effect on the electron temperature in the upper laser state, because electrons with high in-plane momenta quickly relax to the lower laser level, while electrons with lower in-plane momenta have longer lifetime in the upper state and thermalize with the remaining electrons via electron–electron scattering processes. An evidence of this effect can be seen in the simulation results of [20] and [21], which indicate that the electron temperature in the upper laser state is lower than that in the injector states. Since the optical phonon scattering of thermal electrons in the upper laser state is more pronounced at higher temperatures, one may also expect that the difference between the electron temperature in the upper laser state (assuming a thermal distribution there) and the lattice temperature may be reduced at higher operating temperatures.

We have used (8) and (9) to fit the experimental data assuming the electron temperature in the upper laser state is 50 K above the heat sink (lattice) temperature for all laser designs (not shown). The agreement between the experimental data and the fit curve was good with the following fit parameters:

$$\frac{C}{\tau_1} = 90 \text{ A/cm}^2$$
$$\frac{\tau_1}{\tau_{21,\mathrm{hot}}} = 2.9$$

which are even closer to the numbers expected from known laser parameters for THz QCLs as discussed above.

VII. Predicting the J_{TH} Dependence on Temperature for a Diagonal Transition Laser Design

We have shown that, with realistic input parameters, our model explains the temperature behavior of J_{th} in all the devices tested in this work. Given the (semi-)empirical nature of the model, a natural question is whether it can be applied to other laser designs. We show now that (9) describes equally well the temperature behavior of a 3QW design based on the spatially diagonal transition reported in [5].

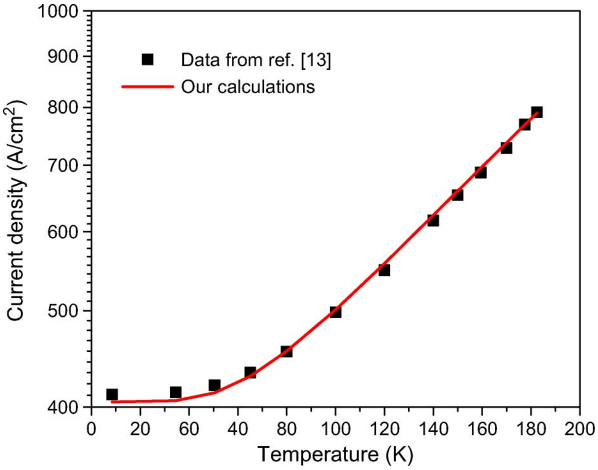

Fig. 8. Application of our model (red curve) to the data from reference [5], reporting operation of a THz QC laser up to a $T_{\max}$ of 186 K. The parameters use to apply Eq. (9) to the structure are taken from Ref. [5]: $N = 3 \times 10^{10}$ cm^{-2}, $\Delta_{1'2} = 0.52$ meV. This yields $J_{\mathrm{par}} = 405$ Acm^{-2}, and $u = (5.9/3.7)^2 = 2.54$. The frequency used is $\nu = 3.9$ THz (necessary to infer the temperature dependence). The agreement of our model with the data is excellent.

The upper and lower laser state wavefunctions in diagonal transition laser designs are spatially separated to a certain extent [5]. As a result, the transition dipole moment and optical phonon scattering rates of thermal electrons in the upper laser state are reduced. We define the following parameter:

$$u = \left[\frac{z_{\mathrm{vertical}}}{z_{\mathrm{diagonal}}}\right]^2$$

where z_{vertical} and $z_{diagonal}$ are the dipolar matrix elements for the vertical and diagonal 3QW resonant-phonon depopulation laser designs, respectively, at the same emission frequency.

Since C is proportional to $1/z^2$, we need to replace C with $C \cdot u$ in our model. The value of $\tau_{21,\mathrm{hot}}$ needs to be modified also. It can be shown (see, e.g., [22]) that the LO-phonon emission rate depends on a form factor which is approximately proportional to z^2 (we have also verified that, in our case, this approximation is correct within 10% of the real value). We can therefore replace $\tau_1/\tau_{21,\mathrm{hot}}$ with $\tau_1/\tau_{21,\mathrm{hot}} \cdot u^{-1}$ in (9). The value of the electron extraction time in the lower laser level, τ_1, as well as the length of the laser period (L_{per}), are approximately the same in the two designs [see (6)]. The value of J_{par} can be estimated with (1) using a sheet doping density $N = 3 \times 10^{10}$ cm^{-2} [5] and the anticrossing energy $\Delta_{1'2} = 0.52$ meV [5] between the ground level of the injector ($1'$) with the first excited level (2) of the injector downstream at a bias voltage that corresponds to the parasitic alignment, see Fig. 5. We obtain $J_{\mathrm{par}} = 405$ Acm^{-2}. Comparing transition dipole moments in our 3.8-THz vertical-transition devices with that reported for a device in [5], we obtain $u = 2.54$. We can now calculate (9) for the devices in [5].

The result is represented by the red curve shown in Fig. 8, which is in good agreement with the experimental data (black diamonds) of [5]. We emphasize that no adjustable parameters have been used here to predict the dependence of $J_{\rm th}$ on temperature for the devices in [5].

VIII. Further Insights Towards Performance Improvement

Our model indicates that one of the fundamental limiting factors in the temperature-performance of resonant-tunneling designs based on a spatially vertical laser transition is the ratio $\tau_1/\tau_{21,\rm hot}$. This ratio is related to the LO-phonon emission rate by hot electrons and the electron extraction time from the lower laser state by resonant tunneling. For our current designs, which experimentally achieve the highest operation temperatures for 3QW THz QCLs based on vertical transitions, we obtain $\tau_1/\tau_{21,\rm hot} \approx 3.4$. According to (7), this implies that nonradiative transition time τ_{21} becomes smaller than the lifetime of the lower laser state τ_1 at temperatures above $T_{\rm lim}$, which is given as

$$T_{\rm lim} \approx \frac{(E_{\rm LO} - h\nu)}{k_B \ln\left(\frac{\tau_1}{\tau_{21,\rm hot}}\right)} \approx \frac{(E_{\rm LO} - h\nu)}{k_B \ln(3.4)}. \tag{10}$$

We have neglected $1/\tau_{12,0}$ in (7) to derive (10). When $\tau_1 < \tau_{21}$, lasing is not possible in principle, even at infinite current densities flowing through the device. Equation (10) yields $T_{\rm lim}$ of $\approx$260 K for 2-THz devices and $T_{\rm max}$ of only $\approx$187 K for 4 THz devices. The maximum current density which can be injected in a real device if of course limited. Therefore, especially for lower frequency THz QCLs (see Figs. 6 and 7 which are most affected by the presence of a parasitic current channel, $T_{\rm max}$ is lower than $T_{\rm lim}$.

THz QCLs based on diagonal laser transitions [5], [10], are free from this fundamental limitation as one can increase the value of $\tau_{21,hot}$ with the diagonality parameter u (see discussion in Section VII). For the laser design reported in [5] and discussed in the previous section, we obtain $u = 2.54$ and $\tau_1/\tau_{21,hot} \approx 3.4 \times u^{-1} = 1.34$ and, from (10), $T_{\rm lim} \approx 790$ K for such a laser. While this value is much higher than the experimental finding in [5], our model does not identify any fundamental limitation on the temperature performance of THz QCLs based on diagonal laser transitions. In our opinion, this is a promising route towards higher operating temperatures.

Diagonal laser transitions have smaller oscillator strengths and require higher current densities to produce sufficient gain to overcome the waveguide loss. This effect is represented in our model by the requirement of scaling constant C with the diagonality parameter u (see the Section VII). Generally speaking, diagonal transitions require designs with reduced $J_{\rm par}$ and a sufficiently large dynamic range to offer performance superior to vertical ones [25]. However, in addition to the diagonality parameter u, the constant C in our model is also proportional to other parameters such as total waveguide loss and gain linewidth factor $\delta\nu$ [see (6)]. Reducing the gain linewidth and the waveguide loss, while simultaneously increasing the current flow via a suppression of $J_{\rm par}$, may lead to significant improvements in the temperature performance of THz QCLs based on diagonal laser transitions. Note that the scattering-assisted injection scheme [8] is particularly promising for increasing the current though the laser states and reducing the laser transition linewidth.

Increasing the diagonality of the transition (the parameter u in our model) is not the only solution to limit the LO-phonon emission by hot electrons. Equation (10) suggests that semiconductor materials with energetic LO-phonon energies—such as GaN/AlGaN—are another interesting route to explore [26], [27]. InGaAs–AlInAs/InP and antimonide-based systems—such as InAs/AlSb, and InGaAs–GaAsSb—are very appealing as well. Their LO-phonon energy is limited (30–35 meV), but the reduced electronic effective mass yields higher transition dipole moments and lower optical–phonon scattering rates [28], [29], which are crucial to attain higher operating temperatures. Our model indicates, however, that successful high-temperature InGaAs/AlInAs, InAs/AlSb, and InGaAs/GaAsSb THz QCL designs have to be based on diagonal laser transitions.

Finally, backfilling of the lower laser state by the electrons from the QCL injector plays a major detrimental role to the THz QCL performance at operating temperatures above 200 K. These effects are not included in our model and they can be effectively suppressed using THz QCL designs using double-phonon depopulation [9].

None of the aforementioned solutions is *the* solution to achieve room-temperature operation of THz QC lasers. Instead, a carefully designed combination of all of the discussed strategies is in our opinion the way forward to major improvements in performance.

IX. Conclusion

In summary, we have studied the temperature performance of THz QCLs based on a 3QW design [11] as a function of their operating frequency. We tested five devices with design frequencies in the range 2.3–3.8 THz. All devices demonstrated very good temperature performance, comparable or better than the current state of the art. We have developed a semi-empirical model which provides an excellent fit to the observed dependence of $J_{\rm th}$ on temperature for all of the devices. The model proposes that the performance of resonant-phonon depopulation THz QCLs is limited by the interplay of two factors: 1) optical-phonon scattering of thermal electrons, which dominates at shorter wavelengths and 2) parasitic current, which dominates at longer wavelengths. We have demonstrated that the model is capable of predicting the dependence of threshold current density on temperature for other device designs, such as 3QW THz QCLs based on diagonal laser transition [5]. The important result of this paper is experimental: data on *several* different lasers exhibit what appears to be a universal behavior which—furthermore—a very simple semi-empirical model can reproduce. Detailed theoretical analysis of the laser performance is needed to fully understand the observed trends. This publication, however, provides the scientific community with the experimental observations and observed trends to foster developing a more in-depth comprehension of the mechanisms which limit the high-temperature operation of current THz QCLs.

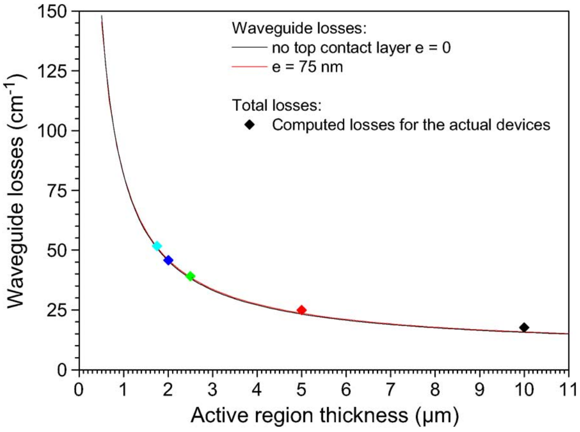

Fig. 9. Waveguide propagation losses α_{wg} (lines) and total optical losses α_{total} (diamonds) as a function of the active region thickness for each measured device. The mirror losses have been calculated using a finite-element approach.

APPENDIX

Here, we investigate five laser devices with different active region thicknesses (t_{AR}) but identical laser design. A GaAs/Al$_{0.15}$Ga$_{0.85}$As THz QCL structure operating at a frequency of 3.1 THz has been used [24]. We show here that the systematic study of these devices allows one to infer the variation of J_{par} as a function of the applied bias. The results suggest that assuming J_{par} as constant above the parasitic alignment is a reasonable approximation for our simple model.

Three wafers were grown by MBE with $t_{\mathrm{AR}} = 10, 5, 2.5\ \mu$m (samples L421, L420, and L422, respectively). The layer structure corresponds to the 3.1-THz design given in Section II. Differences between the 10-μm-thick device presented here and the one presented in the main body of the article can be explained by the rather long time elapsed between the two growth campaigns. Careful wet chemical etching of the 2.5-μm-thick wafer provided two further samples with $t_{\mathrm{AR}} = 2$ and 1.75 μm, albeit sacrificing the 50-nm doped contact layer. All of the devices have been processed into standard metal–metal ridge waveguides.

For the five measured THz devices, the reduction of the active core thickness yields a controlled increase in the waveguide losses (α_{wg}), and it offers the opportunity to perform a systematic study of the laser threshold. The total optical losses (α_{total}) are the sum of mirrors and waveguide losses, but α_{wg} is the dominant contribution in the case of thin metal–metal waveguides. We have calculated—using a 1-D transfer-matrix approach—the evolution of α_{total} in metal–metal waveguides as a function of the AR and top contact layer thickness. The result is reported in Fig. 9 for five different active region thicknesses (diamond symbols). Also shown in Fig. 9 is the dependence of α_{wg} as a function of the active region thickness for devices with and without a thin top contact layer. The results indicate that a thin contact layer has negligible effect on α_{wg} and therefore $\alpha_{\mathrm{wg}} \approx \alpha_{\mathrm{total}}$.

The devices have been characterized in pulsed mode with 300-ns current pulses and duty cycles $\leq 1\%$. The current density as a function of the *total applied bias* at 10 K for each device is shown in the top graph of Fig. 10. The threshold current density increases when t_{AR} decreases, as expected (see the arrows in Fig. 10, bottom panel, and Fig. 11, top panel).

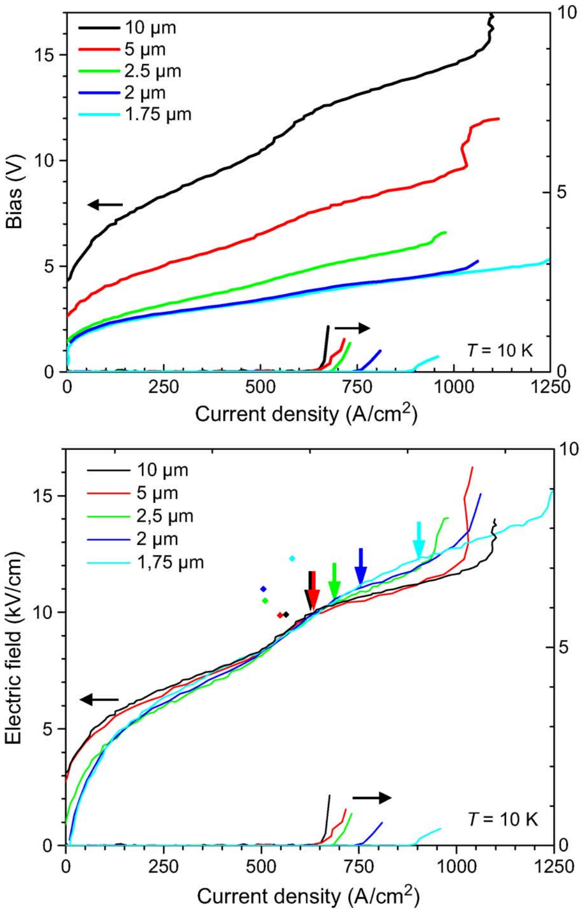

Fig. 10. Top: L–J–V characteristics for all of the measured devices with $t_{\mathrm{AR}} = 10, 5, 2.5, 2$, and 1.75 μm at 10 K. Bottom: L–J–E characteristics for all the measured devices with $t_{\mathrm{AR}} = 10, 5, 2.5, 2$, and 1.75 μm at 10 K. Diamonds indicate the values of J_{par} obtained from fitting the experimental J_{th} at low temperature using (9) and the theoretically calculated values for α_{wg}.

The current density as a function of the applied *electric field* at 10 K for each device is shown in the bottom graph of Fig. 10, as obtained from the top graph in Fig. 10 upon scaling with the AR thickness. We have taken into account the cable resistance and the increased voltage barrier ($\sim$0.15 V) in the 1.75 and 2-μm thinned samples due to the missing top doped contact layer. The maximum of differential resistance at $J_{\mathrm{par}} \approx 550$ Acm^{-2} is consistent for all t_{AR} and it shows the equivalence of the active region in each device.

The top panel of Fig. 11 shows the temperature dependence of J_{th} for all of the five devices with different t_{AR}. Despite different temperature dependences, the value of J_{par} *at the parasitic alignment* (~ 9 kVcm^{-1}) is expected to stay the same since it depends only on the QC laser band structure. However, the increase in J_{th} with decreasing laser thickness offers the opportunity to infer the value of J_{par} for different applied fields. Following (5), we can write

$$J_{\mathrm{th}} = J_{\mathrm{par}} + \frac{\alpha_{\mathrm{total}}}{\Gamma \cdot g_{\mathrm{th}}} \qquad (11)$$

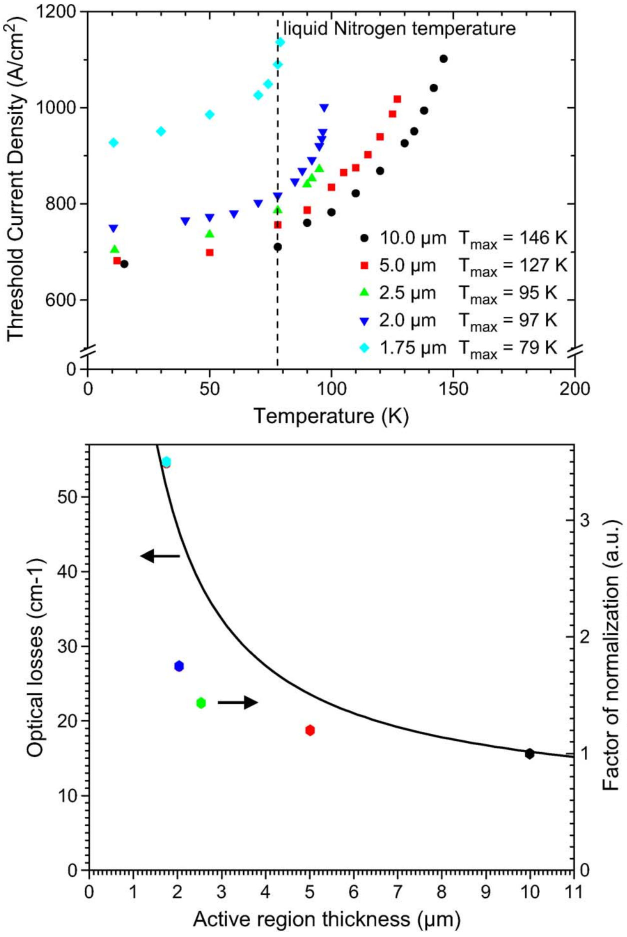

Fig. 11. Top: J_{th} as a function of the heat-sink temperature for all of the measured devices. Bottom: Comparison between α_{total} as obtained using (9) and the experimentally measured J_{th} (values at 10 K for all of the devices), and the theoretical values for the total losses.

If we consider J_{par} constant we can infer the dependence of α_{total} on the AR thickness, since we experimentally measure J_{th} as a function of t_{AR}. The result is reported in Fig. 11, bottom panel, where we have fixed the value of α_{total} at $t_{AR} = 10$ μm equal to the theoretical optical losses of 16 cm^{-1}. While the result is excellent for $t_{\mathrm{AR}} = 10$ μm and 1.75 μm, we apparently overestimate the losses for intermediate values of AR thicknesses. We believe the difference between theory and simulations stems from the fact that J_{par} is not rigorously constant.

If in (5) we consider instead J_{par} as the variable, and we employ the values of α_{total} provided by the calculation, we can instead infer the parasitic current value for different AR thicknesses, and therefore *for different applied fields*. The diamond symbols in Fig. A-2, bottom panel represent the J_{par} obtained with this procedure for each device. It appears that J_{par} slightly decreases after the parasitic alignment and it then increases again.

The minimum and maximum J_{par} values obtained with this method are 500 Acm^{-2} and 570 Acm^{-2}. The hypothesis of constant J_{par} that we have employed in the paper is therefore correct within a 10% error. The analysis suggests that while J_{par} is not strictly constant over the laser dynamic range, the error committed is minor and it is justified given the simplicity of the proposed model.

ACKNOWLEDGMENT

The authors would like to thank R. Ferreira for useful discussions. The device fabrication has been performed at the nanocenter CTU-IEF-Minerve, which is supported in part by the "Conseil Général de l'Essonne", and at the Center for Nanoscale Science (CNS) at Harvard University, Cambridge, MA.

REFERENCES

[1] B. S. Williams, "Terahertz quantum cascade lasers," *Nature Photon.*, vol. 1, pp. 517–525, 2007.
[2] R. Köhler, A. Tredicucci, F. Beltram, E. H. Beere, E. H. Linfield, A. G. Davies, D. A. Ritchie, R. C. Iotti, and F. Rossi, "Terahertz semiconductor heterostructure laser," *Nature*, vol. 417, p. 157, 2002.
[3] S. Barbieri, J. Alton, H. E. Beere, E. H. Linfield, D. A. Ritchie, S. Withington, G. Scalari, L. Ajili, and J. Faist, "Heterodyne mixing of two far-infrared quantum cascade lasers by use of a pointcontact Schottky diode," *Opt. Lett.*, vol. 29, pp. 1632–1634, 2004.
[4] J. R. Gao, J. N. Hovenier, Z. Q. Yang, J. J. Baselmans, A. Baryshev, M. Hajenius, T. M. Klapwijk, A. J. L. Adam, T. O. Klaassen, B. S. Williams, S. Kumar, Q. Hu, and J. L. Reno, "A terahertz heterodyne receiver based on a quantum cascade laser and a superconducting bolometer," *Appl. Phys. Lett.*, vol. 86, 2005, Art. ID 244104.
[5] S. Kumar, Q. Hu, and J. L. Reno, "186 K operation of terahertz quantum-cascade lasers based on a diagonal design," *Appl. Phys. Lett.*, vol. 94, 2009, Art. ID 131105.
[6] B. S. Williams, S. Kumar, Q. Hu, and J. L. Reno, "Operation of terahertz quantum-cascade lasers at 164 K in pulsed mode and at 117 K in continuous-wave mode," *Opt. Exp.*, vol. 13, pp. 3331–3339, 2005.
[7] A. Wade, G. Fedorov, D. Smirnov, S. Kumar, B. S. Williams, Q. Hu, and J. L. Reno, "Magnetic-field-assisted terahertz quantum cascade laser operating up to 225 K," *Nature Photon*, vol. 3, pp. 41–45, 2009.
[8] S. Kumar, C. W. I. Chan, Q. Hu, and J. L. Reno, "A 1.8-THz quantum cascade laser operating significantly above the temperature of $\hbar\omega/k_B$," *Nature Phys.*, vol. 7, p. 166, 2011.
[9] R. W. Adams, K. Vijayraghavan, Q. J. Wang, J. Fan, F. Capasso, S. P. Khanna, A. G. Davies, E. H. Linfield, and M. A. Belkin, " GaAs/Al$_{0.15}$Ga$_{0.85}$As terahertz quantum cascade lasers with double-phonon resonant depopulation operating up to 172 K," *Appl. Phys. Lett.*, vol. 97, 2010, Art. ID 131111.
[10] M. A. Belkin, Q. J. Wang, C. Pfügl, F. Capasso, A. Belyanin, S. Khanna, A. G. Davies, and E. Linfield, "High temperature operation of terahertz quantum cascade laser sources," *IEEE J. Sel. Top. Quantum Electron.*, vol. 15, no. 3, pp. 952–967, May–Jun. 2009.
[11] H. Luo, S. R. Laframboise, Z. R. Wasilewski, G. C. Aers, H. C. Liu, and J. C. Cao, "Terahertz quantum-cascade lasers based on a three-well active module," *Appl. Phys. Lett.*, vol. 90, 2007, Art. ID 041112.
[12] M. A. Belkin, J. Fan, S. Hormoz, F. Capasso, S. Khanna, M. Lachab, A. G. Davies, and E. H. Linfield, "Terahertz quantum cascade lasers with copper metal-metal waveguides operating up to 178 K," *Opt. Exp.*, vol. 16, p. 3242, 2008.
[13] R. F. Kazarinov and R. A. Suris, "Possibility of the amplification of electromagnetic waves in a semiconductor with a superlattice," *Soviet Phys.—Semicond.*, vol. 5, pp. 707–709, 1971.
[14] C. Sirtori, F. Capasso, J. Faist, A. L. Hutchinson, D. L. Sivco, and A. Y. Cho, "Resonant tunneling in quantum cascade lasers," *IEEE J. Quantum Electron.*, vol. 34, no. 9, pp. 1722–1729, Sep. 1998.
[15] T. Kubis and P. Vogl, "Predictive quantum theory of current and optical gain in quantum cascade lasers," *Laser Phys.*, vol. 19, p. 762, 2009.
[16] T. Kubis, C. Yeh, P. Vogl, A. Benz, G. Fasching, and C. Deutsch, "Theory of nonequilibrium quantum transport and energy dissipation in terahertz quantum cascade lasers," *Phys. Rev. B.*, vol. 79, 2009, Art. ID 195323.
[17] M. S. Vitiello, G. Scamarcio, V. Spagnolo, B. S. Williams, S. Kumar, and Q. Hu, "Measurement of subband electronic temperatures and population inversion in THz quantum-cascade lasers," *Appl. Phys. Lett.*, vol. 86, 2005, Art. ID 111115.
[18] C. Jirauschek, G. Scarpa, P. Lugli, M. S. Vitiello, and G. Scamarcio, "Comparative analysis of resonant phonon THz quantum cascade lasers," *J. Appl. Phys.*, vol. 101, 2007, Art. ID 086109.
[19] R. Ferreira and G. Bastard, "Evaluation of some scattering times for electrons in unbiased and biased single- and multiple-quantum-well structures," *Phys. Rev. B*, vol. 40, p. 1074, 1989.

[20] O. Bonno, J.-L. Thobel, and F. Dessenne, “Modelling of electron-electron scattering in Monte Carlo simulation of quantum cascade lsaers,” *J. Appl. Phys.*, vol. 97, 2005, Art. ID 043702.

[21] H. Callebaut and Q. Hu, “Importance of coherence for electron transport in terahertz quantum cascade lasers,” *J. Appl. Phys.*, vol. 98, 2005, Art. ID 104505.

[22] J. H. Smet, C. G. Fonstad, and Q. Hu, “Intrawell and interwell intersubband transitions in multiple quantum wells for far-infrared sources,” *J. Appl. Phys.*, vol. 79, pp. 9305–9319, 1995.

[23] G. Scalari, M. I. Amanti, M. Fischer, R. Terazzi, C. Walther, M. Beck, and J. Faist, “Step well quantum cascade laser emitting at 3 THz,” *Appl. Phys. Lett.*, vol. 94, 2009, Art. ID 041114.

[24] E. Strupiechonski, D. Grassani, D. Fowler, F. H. Julien, R. Colombelli, S. P. Khanna, L. Li, E. H. Linfield, A. G. Davies, and A. B. Krysa, “Vertical sub-wavelength mode confinement in terahertz and midinfrared quantum cascade lasers,” *Appl. Phys. Lett.*, vol. 98, 2011, Art. ID 101101.

[25] A. Matyas, M. A. Belkin, P. Lugli, and C. Jirauschek, “Temperature performance of terahertz quantum cascade lasers: Vertical versus diagonal designs,” *Appl. Phys. Lett.*, vol. 96, 2010, Art. ID 201110.

[26] E. Bellotti, K. Driscoll, T. D. Moustakas, and R. Paiella, “Monte Carlo simulation of terahertz quantum cascade laser structures based on wide-bandgap semiconductors,” *J. App. Phys.*, vol. 105, 2009, Art. ID 113103.

[27] H. Machhadani *et al.*, “Intersubband absorption of cubic GaN/Al(Ga)N quantum wells in the near-infrared to terahertz spectral range,” *Phys. Rev. B*, vol. 83, 2011, Art. ID 075313.

[28] E. Benveniste, A. Vasanelli, A. Delteil, J. Dvenson, R. Teissier, A. Baranov, A. M. Andres, G. Strasser, I. Sagnes, and C. Sirtori, “Influence of the material parameters on quantum cascade devices,” *Appl. Phys. Lett.*, vol. 93, 2008, Art. ID 131108.

[29] T. Kubis, S. R. Mehrotra, and G. Klimeck, “Design concepts of terahertz quantum cascade lasers: Proposal for terahertz laser efficiency improvements,” *Appl. Phys. Lett.*, vol. 97, 2010, Art. ID 261106.

Y. Chassagneux, photograph and biography not available at the time of publication.

Q. J. Wang, photograph and biography not available at the time of publication.

S. P. Khanna, photograph and biography not available at the time of publication.

E. Strupiechonski, photograph and biography not available at the time of publication.

J.-R. Coudevylle, photograph and biography not available at the time of publication.

E. H. Linfield, photograph and biography not available at the time of publication.

A. G. Davies, photograph and biography not available at the time of publication.

F. Capasso, photograph and biography not available at the time of publication.

M. A. Belkin, photograph and biography not available at the time of publication.

R. Colombelli, photograph and biography not available at the time of publication.